

# An Automatic Technique for Finding and Localizing Externally Attached Markers in CT and MR Volume Images of the Head

Matthew Y. Wang, Calvin R. Maurer, Jr., J. Michael Fitzpatrick,\* *Member, IEEE*, and Robert J. Maciunas

**Abstract**—An image processing technique is presented for finding and localizing the centroids of cylindrical markers externally attached to the human head in computed tomography (CT) and magnetic resonance (MR) image volumes. The centroids can be used as control points for image registration. The technique, which is fast, automatic, and knowledge-based, has two major steps. First, it searches the entire image volume to find one voxel inside each marker-like object. We call this voxel a “candidate” voxel, and we call the object a candidate marker. Second, it classifies the voxels in a region surrounding the candidate voxel as marker or nonmarker voxels using knowledge-based rules and calculates an intensity-weighted centroid for each true marker. We call this final centroid the “fiducial” point of the marker. The technique was developed on 42 scans of six patients—one CT and six MR scans per patient. There are four markers attached to each patient for a total of 168 marker images. For the CT images the false marker rate was zero. For MR the false marker rate was 1.4% (Two out of 144 markers). To evaluate the accuracy of the fiducial points, CT-MR registration was performed after correcting the MR images for geometrical distortion. The fiducial registration accuracy averaged 0.4 mm and was better than 0.6 mm for each of the eighteen image pairs.

## I. INTRODUCTION

**D**IFFERENT imaging modalities provide different types of information that can be combined to aid diagnosis and surgery. Bone, for example, is seen best on X-ray computed tomography (CT) images, while soft-tissue structures are seen best on magnetic resonance (MR) images. Because of the complementary nature of the information in these two modalities, the registration of CT images of the head with MR images is of growing importance for diagnosis and for surgical planning. Furthermore, registration of images with patient anatomy is used in new interactive image-guided surgery techniques to track in real time the changing position of a surgical instrument or probe on a display of preoperative image sets of the patient [21], [23], [34]. We define registration as the determination of

Manuscript received May 26, 1995; revised January 12, 1996. Portions of this work were presented at the *15th Annu. Int. Conf. IEEE Eng. Med. Biol. Soc. (1993)* and the *SPIE Conf., Med. Imag. 1994*. Asterisk indicates corresponding author.

M. Y. Wang is with the Departments of Computer Science and Neurological Surgery, Vanderbilt University, Nashville, TN 37235 USA.

C. R. Maurer, Jr. is with the Departments of Biomedical Engineering and Neurological Surgery, Vanderbilt University, Nashville, TN 37235 USA.

\*J. M. Fitzpatrick is with the departments of Computer Science, Neurological Surgery, and Radiology, Vanderbilt Univ., Box 1679, Station B, Nashville, TN 37235 USA (e-mail: jmf@vuse.vanderbilt.edu).

R. J. Maciunas is with the Department of Neurological Surgery, Vanderbilt University, Nashville, TN 37232 USA.

Publisher Item Identifier S 0018-9294(96)03990-0.

a one-to-one mapping between the coordinates in one space and those in another, such that points in the two spaces that correspond to the same anatomic point are mapped to each other.

Many methods have been used to register medical images [40], [53]. In this paper we are primarily concerned with point-based registration. Point-based registration involves the determination of the coordinates of corresponding points in different images (and/or physical space) and the estimation of the geometrical transformation using these corresponding points [36], [41]. The points may be either intrinsic [16], [18], [27] or extrinsic [10], [17]–[19], [28], [30], [33], [36], [41], [47], [54]. Intrinsic points are derived from naturally occurring features, e.g., anatomic landmark points. Extrinsic points are derived from artificially applied markers, e.g., tubes containing copper sulfate. We use external fiducial markers that are rigidly attached through the skin to the skull [36], [41]. We call the points used for registration *fiducial points* or *fiducials*, as distinguished from “fiducial markers,” and pick as the fiducials the geometric centers of the markers.

Determining the coordinates of the fiducials, which we call *fiducial localization*, may be done in image space or in physical space. Several techniques have been developed for determining the physical space coordinates of external markers. Examples include articulated arms [1], [23], [33], [49], optical triangulation systems [22], magnetic field digitizers [30], and ultrasonic range finders [19]. This paper is concerned with determining the CT and MR image space positions of external markers. Image localization can be performed manually, semiautomatically, or fully automatically. Mandava [35], [36] and DeSoto [13] have presented semiautomatic fiducial localization techniques that use adaptive intensity-based segmentation algorithms. In this paper we improve Mandava’s work by applying a more accurate knowledge-based segmentation method, and we automate each step so that no human activity is involved. We include the results of tests with four cylindrical markers on 42 scans of six patients—one CT and six MR scans per patient.

## II. ALGORITHM

### A. Overview

The algorithm finds markers in image volumes of the head. A three-dimensional (3-D) image volume typically consists of a stack of two-dimensional (2-D) image slices. The algorithm

finds markers whose image intensities are higher than their surroundings. It is also tailored to find markers of a given size and shape. All of the marker may be visible in the image, or it may consist of both imageable and nonimageable parts. It is the imageable part that is found by the algorithm, and it is the size and shape of this imageable part that is important to the algorithm. Henceforth when we use the term "marker" we are referring to only the imageable portion of the marker. Three geometrical parameters specify the size and shape of the marker adequately for the purposes of this algorithm: 1) the radius  $r_m$  of the largest sphere that can be inscribed within the marker; 2) the radius  $R_m$  of the smallest sphere that can circumscribe the marker; and 3) the volume  $V_m$  of the marker. In this paper we use cylindrical markers with diameter  $d$  and height  $h$  for clinical experiments. For these markers  $r_m = \min(d, h)/2$ ,  $R_m = \sqrt{d^2 + h^2}/2$ , and  $V_m = \pi d^2 h/4$ .

Our problem is two-fold. First, we must search the entire image volume to find marker-like objects. Second, for each marker-like object, we must decide whether it is a true marker or not and accurately localize the centroid for each true one. Therefore, the algorithm consists of two parts. Part One finds "candidate voxels." Each candidate voxel lies within a bright region that might be the image of a marker. The requirements imposed by Part One are minimal with the result that, for the  $M$  markers in that image, there are typically many more than  $M$  candidate points identified. If, for example,  $M$  is four, Part One might identify eighty candidates. Part Two selects from these candidates  $M$  points that are most likely to lie within actual markers and provides a centroid for each one. Part One is designed so that it is unlikely to miss a true marker. Part Two is designed so that it is unlikely to accept a false marker.

### B. Inputs and Outputs

Part One takes the following input:

- The image volume of the head of a patient.
- The type of image (CT or MR).
- The voxel dimensions  $\Delta x_v$ ,  $\Delta y_v$ , and  $\Delta z_v$ .
- The marker's geometrical parameters  $r_m$ ,  $R_m$ , and  $V_m$ .
- The intensity of an empty voxel.

Part One produces as output a set of candidate voxels.

Part Two takes the same input as Part One, plus two additional pieces of information:

- The set of candidate voxels produced by Part One of the algorithm.
- The number of external markers  $M$  known *a priori* to be present in the image.

Part Two produces as output a list of  $M$  "fiducial points." Each fiducial point is a 3-D position  $(x_f, y_f, z_f)$  that is an estimate of the centroid of a marker. The list is ordered with the first member of the list being most likely to be a marker and the last being the least likely.

### C. The Steps of Part One

Part One operates on the entire image volume. It comprises the following steps (see Figs. 1 and 2)

- 1) If the image is an MR image, a 2-D, three-by-three median filter is applied within each slice to reduce noise.

- 2) To speed up the search, a new, smaller image volume is formed by subsampling [see Figs. 1(a) and 2(a)]. The subsampling rate in  $x$  is calculated as  $\lfloor r_m/\Delta x_v \rfloor$ , where  $\lfloor \cdot \rfloor$  is the floor function. The subsampling rates in  $y$  and  $z$  are similarly calculated.
- 3) An intensity threshold is determined. For CT images, the threshold is the one that minimizes the within-group variance [45]. For MR images, the threshold is computed as the mean of two independently determined thresholds. The first is the threshold that minimizes the within-group variance. The second is the threshold that maximizes the Kullback information value [31].
- 4) This threshold is used to produce a binary image volume with higher intensities in the foreground [see Figs. 1(b) and 2(b)]. Foreground voxels are typically voxels that are part of the image of markers or of the patient's head.
- 5) If the original image is an MR image, spurious detail tends to appear in the binary image produced by the previous step. The spurious detail is composed of apparent holes in the head caused by regions that produce weak signal, such as the skull and sinuses. Thus, if the original image is an MR image, these holes in the binary image are filled [see Figs. 1(c) and 2(c)]. In this step each slice is considered individually. A foreground component is a two-dimensionally connected set of foreground voxels. The holes are background regions completely enclosed within a slice by a single foreground component. This step reduces the number of false markers.
- 6) Two successive binary, 2-D, morphological operations are performed on each slice [see Figs. 1(d), 1(e), 2(d), and 2(e)]. The operations taken together have the effect of removing small components and small protrusions on large components. In particular, the operations are designed to remove components and protrusions whose cross sections are smaller than or equal to the largest cross section of a marker. The operations are erosion and dilation, in that order. The structuring element is a square. The  $x$  dimension (in voxels) of the erosion structuring element is calculated as  $\lceil 2R_m/\Delta x'_v \rceil$ , where  $\lceil \cdot \rceil$  is the ceiling function and the prime refers to the subsampled image. The  $y$  dimension is similarly calculated. The size of the dilation structuring element in each dimension is the size of the erosion element plus one.
- 7) The binary image that was output by the previous step is subtracted from the binary image that was input to the previous step [see Figs. 1(f) and 2(f)]. That is, a new binary image is produced in which those voxels that were foreground voxels in the input image but background in the output image are set to foreground. The remaining voxels are set to background. The result is a binary image consisting only of the small components and protrusions that were removed in the previous step.
- 8) For the entire image volume, the foreground is partitioned into 3-D connected components. The definition of connectedness can be varied. We have found that including the eight 2-D eight-connected neighbors within the slice plus the two 3-D six-connected neighbors on

the neighboring slices works well for both CT and MR images.

- 9) The intensity-weighted centroid of each selected component is determined using the voxel intensities in the original image. The coordinates of the centroid position  $(x_c, y_c, z_c)$  are calculated independently as follows

$$x_c = \frac{\sum_i (I_i - I_0) x_i}{\sum_i (I_i - I_0)}$$

$$y_c = \frac{\sum_i (I_i - I_0) y_i}{\sum_i (I_i - I_0)}$$

$$z_c = \frac{\sum_i (I_i - I_0) z_i}{\sum_i (I_i - I_0)}$$

The sums are taken over all voxels in the component. The value  $I_i$  is the intensity of voxel  $i$ ;  $I_0$  is the intensity of an empty voxel; and  $x_i, y_i,$  and  $z_i$  are the coordinates of the center of voxel  $i$ .

- 10) The voxels that contain the points  $(x_c, y_c, z_c)$  are identified.

The voxels identified in the last step are the candidate voxels.

#### D. The Steps of Part Two

Part Two operates on a region of the original image (i.e., not the subsampled image) around each candidate voxel. We desire to use the smallest region possible to improve speed. The region must contain all voxels whose centers are closer to the center of the candidate voxel than the longest marker dimension ( $2R_m$ ), plus all voxels that are adjacent to these voxels [see rule (a) in Step 1) below]. For convenience, we use a rectangular parallelepiped that is centered about the candidate voxel. The  $x$  dimension (in voxels) is calculated as  $2[2R_m/\Delta x_v] + 3$ . The 3 represents the center voxel, plus an adjacent voxel on each end. The  $y$  and  $z$  dimensions are similarly calculated. For each of these regions Part Two performs the following steps

- 1) It is determined whether or not there exists a "suitable" threshold for the candidate voxel. This determination can be made by a brute-force checking of each intensity value in the available range of intensities. We use instead a more efficient binary search strategy. In either case a suitable threshold is defined as follows. For a given threshold the set of foreground (higher-intensity) voxels that are three—dimensionally connected to the candidate voxel are identified. We use the same connectedness as in Step 8) of Part One. The threshold is considered suitable if the size and shape of this foreground component is sufficiently similar to that of a marker. There are two

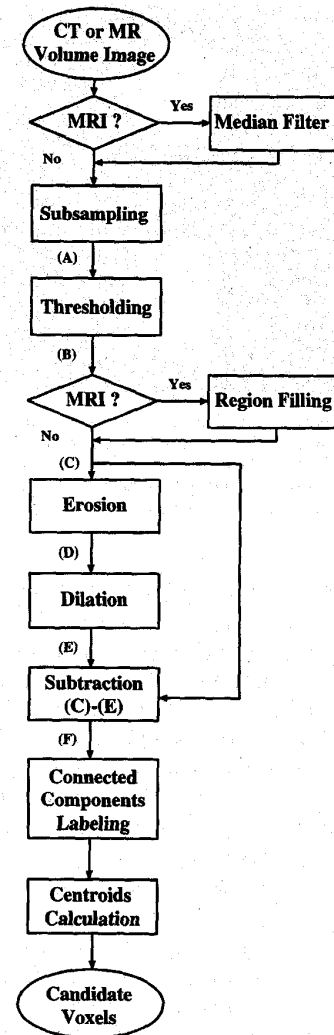


Fig. 1. Schematic outline of Part One of the localization algorithm. The labels (a) through (f) refer to sample images in Fig. 2. See the text for details.

rules that determine whether the size and shape of the component are sufficiently similar.

- a) The distance from the center of the candidate voxel to the center of the most distant voxel of the component must be less than or equal to the longest marker dimension ( $2R_m$ ).
  - b) The volume,  $V_c$ , of the component, determined by counting its voxels and multiplying by the volume of a single voxel  $V_v = \Delta x_v \times \Delta y_v \times \Delta z_v$ , must be within the range  $[\alpha V_m, \beta V_m]$ . See the Section VI for information about factors influencing the choice of the values of  $\alpha$  and  $\beta$ .
- 2) If no such threshold exists, the candidate point is discarded. If there are multiple suitable thresholds, the smallest one (which produces the largest foreground component) is chosen in order to maximally exploit the intensity information available within the marker.

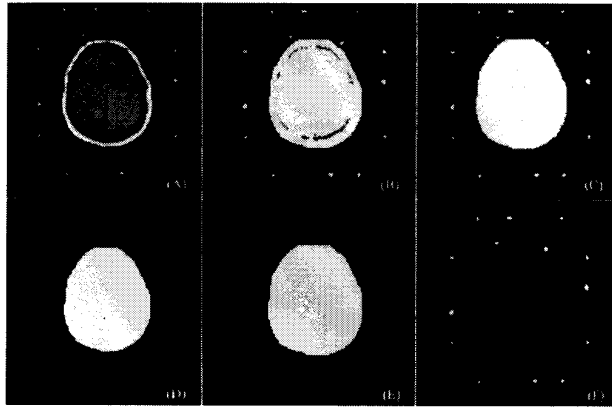


Fig. 2. Sample image slices produced after various steps of Part One of the localization algorithm. The input volume image is an MR T1-weighted Spin-Echo scan. The image labels correspond to labels in Fig. 1. The images were produced after (a) subsampling, (b) thresholding, (c) region filling, (d) erosion, (e) dilation, and (f) subtraction of (e) from (c).

- 3) If the threshold does exist, the following steps are taken.
  - a) The intensity-weighted centroid of the foreground component is determined using the voxel intensities in the original image. The coordinates of the centroid position  $(x_f, y_f, z_f)$  are calculated as in Step 9) of Part One of the algorithm but with the foreground component determined in Step 1).
  - b) The average intensity of the voxels in the foreground component is calculated using the voxel intensities in the original image.
- 4) The voxel that contains the centroid  $(x_f, y_f, z_f)$  is iteratively fed back to Step 1 of Part Two. If two successive iterations produce the same centroid, the centroid position and its associated average intensity is recorded. If two successive iterations have not produced the same centroid by the fourth iteration, the candidate is discarded.

The centroid positions  $(x_f, y_f, z_f)$  are ranked according to the average intensity of their components. The  $M$  points with the highest intensities are declared to be fiducial points and are output in order by rank. A candidate with a higher intensity is considered more likely to be a fiducial point.

### III. EXPERIMENTAL METHODS

#### A. Image Acquisition

We use X-ray, CT, and MR head image volumes acquired from six patients that underwent craniotomies in a stereotactic neurosurgical clinical trial. Each patient had four external markers attached to posts screwed into the outer table of the skull. Each patient also had a COMPASS stereotactic head frame (Stereotactic Medical Systems, Inc., Rochester, MN) applied. The base ring of the frame was attached to the bed of the scanner during image acquisition. (The frame is a redundant reference system and was ignored for our purposes. Nonetheless, it also serves as a head fixation device.) The

CT images were acquired using a Siemens DR-H scanner. Each CT image contained between 27 and 34 slices that were 4 mm thick; each slice contained  $512 \times 512$  pixels of size  $0.65 \times 0.65$  mm. The MR images were acquired using a Siemens SP 1.5 Tesla scanner. Images were obtained using the body coil (because the stereotactic frame will not fit within the head coil). Each MR image contained either 20 or 26 slices that were 4 mm thick (with no interslice gap); each slice contained  $256 \times 256$  pixels of size  $1.25 \times 1.25$  mm. Transverse T1-weighted (T1), proton density-weighted (PD), and T2-weighted (T2) Spin-Echo images were acquired for each patient. The imaging parameters for the T1 images were TE = 15 ms, TR = 650 or 800 ms, readout gradient magnitude = 2.45 mT/m, slice selection gradient magnitude = 6.8 mT/m, four acquisitions, and half-Fourier reconstruction [26], [37]. The imaging parameters for the dual echo PD/T2 images were TE = 20/90 ms, TR = 2550 or 3000 ms, readout gradient magnitude = 1.47 mT/m, slice selection gradient magnitude = 6.8 mT/m, two acquisitions, and half-Fourier reconstruction. Three additional MR images were acquired for each patient with the identical imaging parameters except that the readout gradient was reversed. Acquisition takes approximately eight (14) min for each T1 (PD/T2) image. The patient is in the MR scanner for approximately one hour (including patient setup and scout image acquisition).

#### B. Geometrical Distortion Correction

We have shown that correction of geometrical distortion in MR images can significantly improve the accuracy of point-based, surface-based, and frame-based registration [14], [38], [39]. The MR images are corrected for scale distortion by using the COMPASS stereotactic frame as an object of known shape and size. The MR images are corrected for static field inhomogeneity by using the pair of distorted images acquired with reversed readout gradients. It is possible to do full "image" rectification as detailed in [6], [7], [38], and [39]. We instead perform "point" rectification as described in [14].

#### C. Markers

The markers were designed to be bright in both CT and MR images (see Fig. 3). They are constructed from hollow plastic cylinders with an inside diameter  $d = 7$  mm and an inside height  $h = 5$  mm (see Fig. 4). The values of the geometrical parameters defined in Section II-A are  $r_m = 2.5$  mm,  $R_m = 4.3$  mm, and  $V_m = 192 \mu\text{l}$ . The cylinders are filled with an aqueous solution of 165-mg/ml iohalamate meglumine and 0.5-mM gadopentetate dimeglumine and sealed. The marker is bright in CT images because iodine attenuates X-rays. The marker is bright in MR images because gadolinium reduces the T1 relaxation parameter of the hydrogen protons in the water.

Markers are implanted after obtaining informed consent in accordance with Institutional Review Board approved clinical protocol guidelines. Implantation sites are selected on an individual basis, depending on clinical circumstances. One milliliter of local anesthetic is instilled subcutaneously at each site to minimize discomfort during application. After making

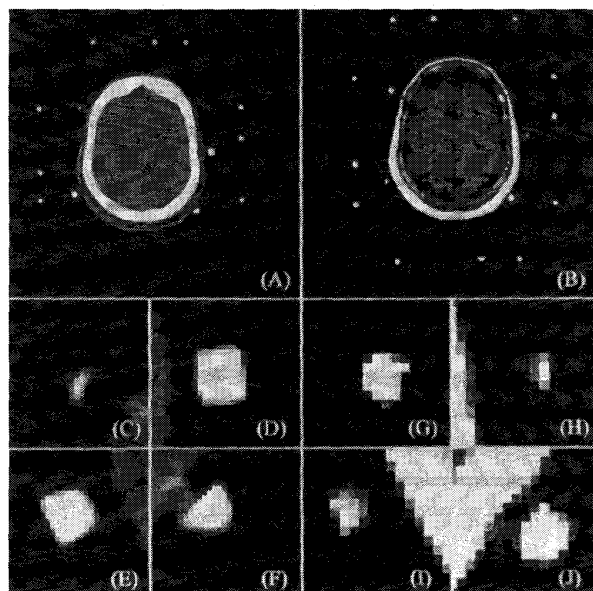


Fig. 3. Appearance of the marker in CT and MR T1-weighted Spin-Echo images. Images (a) and (b) show transverse CT and MR image slices, respectively, of the head. Four markers appear in these slices. The markers are close to the skin. The nine (a) or 12 (b) dots in the image periphery are cross sections of the stereotactic frame N-bars. Thin plastic protective covers are faintly visible in the CT images. Images (c) through (f) are enlargements of the four markers in image (a); images (g) through (j) are enlargements of the four markers in image (b).

a 3.5-mm skin incision, a sterile guide is advanced to the outer table of the skull and a premeasured drill is inserted to produce a 4-mm-deep anchoring hole. An applicator, preloaded with a marker base, is advanced down the guide cannula and the base is screwed into the bone of the skull. The plastic marker base is 13 mm in length and 3 mm in diameter; the threaded end is 3 mm in length (see Fig. 4). Marker bases may remain in place for weeks at a time. The markers are attached to the bases during image acquisition. Patients can undergo surgery at any time after image acquisition. There is a risk of superficial infection at the implantation sites. Strict aseptic technique is utilized throughout the course of all implantations and prophylactic antibiotics are used (they are already routinely administered preoperatively for all neurosurgical procedures). No such infections have been observed in clinical results to date.

#### D. Point-Based Registration

When we use markers to register images, we call them *fiducial markers* and call their positions *fiducial points* or *fiducials*. We register CT and MR images by calculating the rotation and translation parameters of the rigid body transformation that minimizes the mean square distance between corresponding fiducials in the two images [36], [41]. We have implemented the closed-form solution developed by Arun *et al.* [3]. The method decouples the calculations of the rotation and translation parameters. The translation vector is computed as the difference between the centroids of the two sets of

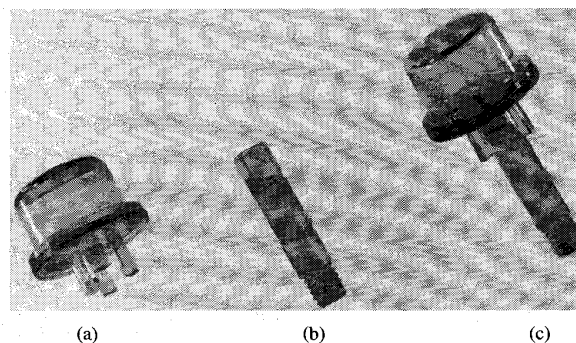


Fig. 4. Photograph of (a) marker. The fiducial markers are constructed from hollow plastic cylinders with an inside diameter  $d = 7$  mm and an inside height  $h = 5$  mm, and thus have an internal volume  $V_m = 192 \mu\text{l}$ . The cylinders are filled with an aqueous solution of 165-mg/ml iohalamate meglumine and 0.5-mM gadopentetate dimeglumine and sealed. The threaded ends of (b) plastic marker bases or posts are screwed into the outer table of the skull of the patient. The marker base is 13 mm in length and 3 mm in diameter; the threaded end is 3 mm in length. The markers are attached to the (c) bases during image acquisition.

fiducials. The rotation matrix is computed using the singular value decomposition of the covariance matrix of the centroid-subtracted position vectors in the two spaces. We define the *fiducial registration error* (FRE) as the root-mean-square (rms) distance between corresponding fiducials after registration and transformation.

#### IV. RESULTS

We developed and tested our automatic localization technique on 42 image volumes from six patients—one CT and six MR (forward and reverse readout gradient T1, PD, and T2) image volumes per patient. There are four markers attached to each patient for a total of 168 marker images (24 in CT, 144 in MR). Using a Silicon Graphics Indy R4400SC/150MHz workstation with sufficient random access memory (RAM) to keep the largest image volume in memory, the processing time averaged 87 s (range = 82–91) per image volume for CT and 18 s (9–48) for MR.

We set the values of  $\alpha$  and  $\beta$  in Step 1-b) of Part Two to  $\alpha = 1.3$  and  $\beta = 2.7$  (CT) or  $\beta = 3.4$  (MR). With these values the algorithm never failed to find a threshold that obeyed the rules in Step 1) of Part Two in any of the 168 fiducial localizations. See Section V for information about factors influencing the choice of the values of  $\alpha$  and  $\beta$ .

In the six CT images, 277 candidate voxels were identified by Part One. Of these candidates all but 35 were discarded by Part Two. After ranking the markers by average intensity and selecting the four markers with the highest average intensity, all 24 true markers were recognized. Thus, the algorithm exhibited a false marker rate of zero for the CT images. We note that because the algorithm is given the number  $M$  of markers, the false positive rate must equal the false negative rate. We refer to both of them as the “false marker” rate. In the 36 MR images, 2237 candidate voxels were identified by Part One. Of these candidates all but 178 were discarded by Part Two. After selecting the four markers with

TABLE I  
SUMMARY OF ALGORITHM PERFORMANCE

Image Modality	Candidates Produced by Part One	Markers Produced by Part Two				False Marker Rate (%)
		Before Ranking		After Ranking		
		True	False	True	False	
CT	277	24	11	24	0	0.0
MR T1	219	48	2	47	1	2.1
MR PD	288	48	3	47	1	2.1
MR T2	1,730	48	29	48	0	0.0
MR Total	2,237	144	34	142	2	1.4
CT & MR Total	2,514	168	45	166	2	1.2

Summary of the output of Parts One and Two of the localization algorithm. For each image modality, this table lists the number of candidate voxels produced by Part One, the number of true and false markers produced by Part Two before and after ranking the markers by average intensity, and the false marker rate. The false marker rate is the number of false markers misidentified as true markers as a percentage of the number of true markers.

the highest average intensity, 142 of the 144 true markers were recognized. Thus, the false marker rate was 1.4% for MR. These results are summarized in Table I. Fig. 5 illustrates a false marker produced by Part Two that was misidentified as a true marker.

In order to test the accuracy of the localization algorithm, CT-to-MR image registration was performed using the four fiducial points in each image. Before registration, compensation for geometrical distortion in the MR images due to static field inhomogeneity and gradient error was applied to each corresponding pair of centroids in the forward and reverse readout gradient images as described in [7], [14], and [42]. Each CT image was thus registered to the geometrically corrected T1, PD, and T2 images from the same patient. The FRE of the 18 registrations was  $0.41 \pm 0.09$  mm [mean  $\pm$  standard deviation (SD)]. The maximum FRE observed was less than 0.6 mm.

The fiducial positions are calculated as intensity-weighted centroids in Step 2-a) of Part Two of the localization algorithm. To investigate the importance of intensity weighting, the FRE was also determined using fiducial positions calculated without intensity weighting. That FRE was  $0.55 \pm 0.18$  mm, which is significantly higher than the FRE determined using intensity-weighted centroids (one-tailed paired *t*-test,  $P = 0.05$ ). Fig. 6 compares the FRE's calculated using intensity-weighted and unweighted fiducial positions. The preponderance of points below the 45° dashed line illustrates the importance of intensity weighting. The three points above the line all came from one patient. There is no significant difference in FRE among the T1, PD, and T2 images (ANOVA,  $P = 0.05$ ).

We tested the sensitivity of the output of Part Two of the algorithm to the candidate voxel input to it by Part One as follows. We ran the algorithm normally and saved every voxel belonging to every marker. Then each of these voxels was used as an input to Part Two. We found that the output of Part Two is completely insensitive to the candidate voxel provided to it. That is, it finds the same fiducial

position regardless of which voxel belonging to the marker was input.

## V. DISCUSSION

A common approach to image matching that might be useful for finding and localizing fiducial markers is the cross-correlation technique, also known as template matching [4], [12], [25], [29]. In its most basic form this method provides pixel accuracy. One way to achieve subpixel accuracy for images that differ only by translation is to calculate the discrete cross-correlation function between two images, fit an interpolation surface to samples of this function, and then search for the maximum of this surface [2], [15]. Another way of achieving subpixel accuracy is to calculate the correlation on a finer grid by interpolating one of the images. Tian and Huhns [51] have shown that using bilinear interpolation, a 0.01–0.05-pixel registration accuracy of 2-D images that differ only by a translation can be achieved. They assume a sampling rate greater than the Nyquist frequency. Since the size of our marker is on the order of the thickness of an image slice, this assumption is violated, and it is unclear what accuracy could be achieved. A cross-correlation approach in our case is also complicated by the fact that a marker has an arbitrary orientation in 3-D space. A marker image and a template image will differ by a rotation as well as a translation, and marker shape in an image slice varies with orientation (see Fig. 7). Interpolating and exhaustively searching a dense grid in transformation parameter space can be computationally demanding, especially in the six-dimensional (6-D) parameter space of a 3-D rigid body transformation. The time requirements can be reduced with an efficient iterative search. Also, functions that are invariant under some of the allowed geometric transformations allow one to reduce the dimension of the parameter space in which the correlation cost function must be optimized. For example, one well known invariant function is the Fourier–Mellin transform, which is translation invariant and represents rotation and scaling

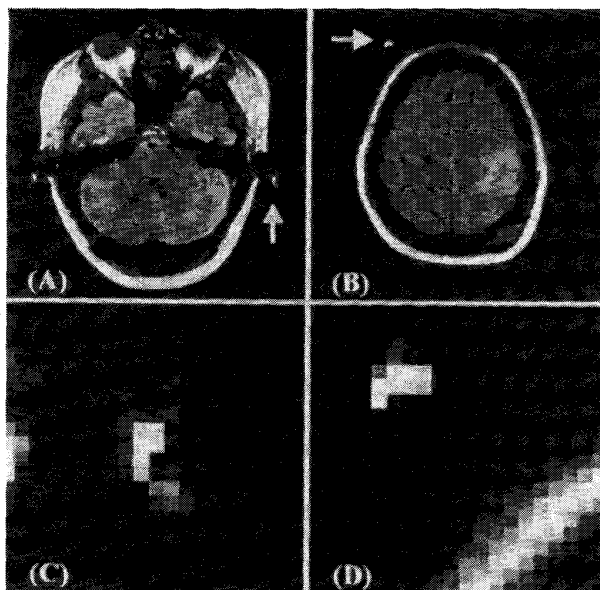


Fig. 5. Misidentified marker in MR proton, density-weighted, Spin-Echo image. The arrows in images (a) and (b) point to a false and a true marker, respectively, produced by Part Two of the localization algorithm. Images (c) and (d) are enlargements of the markers in images (a) and (b). The false marker is a pad of subcutaneous fat in the left ear lobe. It was misidentified as a true marker by Part Two of the localization algorithm after ranking the markers by average intensity and selecting the four markers with the highest average intensity. This false marker is the PD false marker identified by an arrow in Fig. 8.

as translations along the corresponding axes in parameter space [8]. Unfortunately its usefulness is limited to 2-D transformation.

Though a cross-correlation or template-matching approach might be useful for finding and localizing markers, we elected instead to define the fiducial point of the marker as its centroid. This approach requires that we first segment the marker from background and then calculate its intensity-weighted centroid. Our markers were designed to be bright in both CT and MR images, and in the ideal case they lie against a background of air, which does not image. Thus, our segmentation problem should be relatively straightforward: divide the image into marker and background voxels by thresholding; and region-grow connected marker voxels.

Thresholding is complicated by a number of factors. First, the marker is not necessarily the brightest object in the image, though it should be brighter than its immediate surroundings. Second, the intensity of the marker is unknown. The intensity scale of an MR image is variable and unknown. The intensity scale of a CT image is fixed and known, but the maximum intensity of the voxels containing marker will be lower than the expected maximum intensity if no voxel is completely filled with marker. Third, the background is not always air. Sometimes marker voxels are adjacent to skin tissue. Also, the plastic marker housing and post appear, albeit dim, in CT images. For example, the base of a marker can be seen in Fig. 3(c) and (f) (the marker is white, the base is gray). Finally, we wish to set the intensity threshold as low as possible in

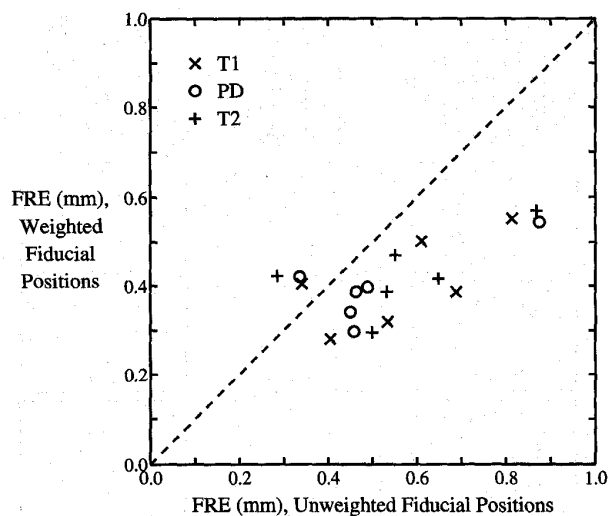


Fig. 6. Comparison of CT-to-MR fiducial registration errors (FRE) determined using fiducial positions calculated with and without intensity weighting. The preponderance of points below the 45° line shows the importance of intensity weighting. The FRE determined using fiducial positions with intensity weighting is  $0.41 \pm 0.09$  mm (mean  $\pm$  SD). The FRE without intensity weighting is  $0.55 \pm 0.18$  mm.

order to maximally exploit the intensity information available within the marker.

Thus we need to use an adaptive thresholding technique. Sahoo [48] and Glasbey [24] review and compare thresholding algorithms. Unfortunately, these techniques generally assume that foreground and background voxels come from two dominant modes. Since the size of the marker is on the order of the thickness of an image slice, many of the voxels containing marker suffer from the partial volume effect, i.e., they contain a mixture of marker and air. Thus the intensity histogram of the image in a region surrounding a marker frequently does not have two dominant modes. Typically it has a dominant mode corresponding to background noise and a widely dispersed region corresponding to foreground marker. The background mode can also be dispersed if it contains tissue or, in the case of CT, a marker post.

For Part One of the algorithm, which locates candidate marker voxels, we found that traditional histogram-based thresholding algorithms are adequate since the exact threshold used is not critical. However, for Part Two, we found that several traditional histogram-based thresholding algorithms, including [31], [32], and [45], produced unreliable thresholds. Sometimes the threshold was set so low that the connected foreground components would attach to the head across a tissue or marker post "bridge." Other times, the threshold was set so high that many voxels that were obviously within a marker by visual inspection were classified as background. Thus we invented the thresholding technique that is the first step of Part Two. The idea is simple, but is, to the best of our knowledge, novel. The technique essentially finds the lowest threshold such that an object formed from voxels whose intensities are higher than the threshold and that are three-dimensionally connected to the candidate marker voxel is neither too small

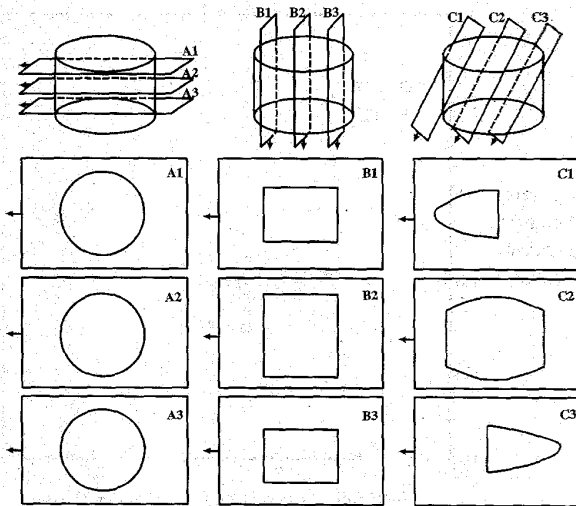


Fig. 7. Variation of marker shape in an image slice with orientation.

nor too large to be a marker. If it is not possible to find such a threshold, the candidate marker is identified as a false marker and rejected. For example, stereotactic frame N-bar cross sections, which appear as marker-like objects in the image periphery [see Fig. 2(a)], are sometimes identified as candidate markers by Part One [see Fig. 2(f)]. But they are rejected by Part Two because an N-bar cross section is three-dimensionally connected to N-bar cross sections in adjacent slices, and it is not possible to find a threshold that satisfies rules 1-a) and 1-b).

The parameters  $\alpha$  and  $\beta$  specify the allowable range of the volume  $V_c$  of a foreground component in terms of the volume  $V_m$  of the marker, i.e.,  $\alpha \leq V_c/V_m \leq \beta$ . We performed numerical simulations in which we randomly varied the position and orientation of a marker and counted the number of voxels the marker partially or completely fills [55]. We found that for the CT image voxel dimensions ( $0.65 \times 0.65 \times 4.0$  mm),  $1.6 \leq V_c/V_m \leq 2.7$  (mean = 2.0); for the MR image voxel dimensions ( $1.25 \times 1.25 \times 4.0$  mm),  $1.7 \leq V_c/V_m \leq 3.4$  (mean = 2.5). Thus we set the value of the parameter  $\beta$  to 2.7 for the CT images and 3.4 for MR. These values are considerably higher than 1.0 because the marker is just slightly larger than the largest voxel dimension and thus many marker voxels are only partially filled. We initially set the value of the parameter  $\alpha$  to 1.6 for the CT images and 1.7 for MR. But with these values of  $\alpha$ , 20 of the 168 markers (12%) were rejected by rule 1-b) of Part Two. Visual inspection of these cases revealed that all 20 rejected markers were adjacent to skin tissue. We found that by using  $\alpha = 1.3$  (CT and MR), no true markers were rejected. By using a smaller value of  $\alpha$ , the algorithm can set a higher threshold and thereby "disconnect" foreground components (marker voxels) from the head.

This thresholding technique will obviously tend to accept intensity "blobs" that have roughly the same size as a marker. To eliminate nonmarker blobs, we exploit the fact that the markers are bright by ranking the centroid positions produced

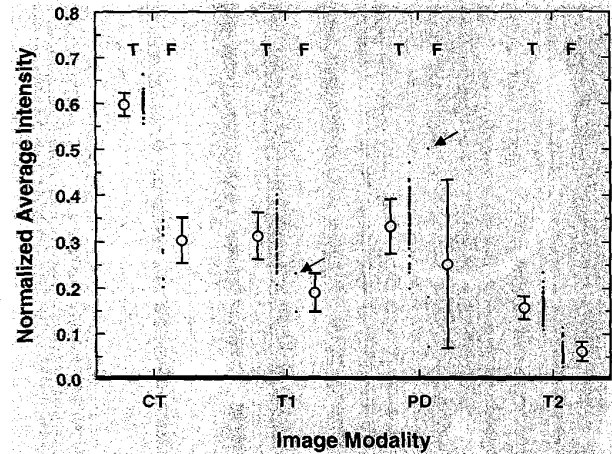


Fig. 8. Normalized average intensities of true (T) and false (F) markers produced by Part Two of the localization algorithm. Because the intensity scale of an MR image is variable and unknown, we normalized the average intensities of markers in MR images to the brightest intensity in the image. We normalized the average intensities of markers in CT images to the intensity of a voxel completely filled with marker (normalization in this case is not necessary because the intensity scale of CT is fixed and known, but we normalized anyway to maintain a single scale in this figure). The small filled circles represent individual intensity values. The open circles with error bars represent means  $\pm$  one SD. The two false markers misidentified as true markers are indicated with arrows. One false T2 marker has a normalized average intensity greater than one true T2 marker, but the false marker was not misidentified since the true T2 marker was from a different patient.

in Part Two according to the average intensity of their component voxels and declaring the  $M$  points with the highest intensities to be fiducial marker positions. In this way we identified 166 of the 168 marker images used in this study. The marker positions produced by the algorithm are reviewed by the user in a graphical interface. False markers are discarded. In this case the user can then examine centroid positions with lower rankings (i.e.,  $M + 1$ ,  $M + 2$ , ...), or interactively provide new candidate voxels for Part Two. We note that the two markers not originally identified were ranked fifth. We also note that Part Two can serve as the engine for a semiautomatic technique in which the user interactively specifies the candidate voxels. The fact that Part Two is completely insensitive to the candidate voxel provided to it means that results using Part Two as a semiautomatic technique will be user independent.

Fig. 8 illustrates the relationship between the average intensities of true and false markers produced by Part Two of the localization algorithm. The algorithm as written takes as input the number of external markers  $M$  known *a priori* to be present in the image. Since there is a large difference between the normalized average intensities of true and false markers, it might be possible to eliminate  $M$  as an input variable.

Fiducial localization error (FLE) is the rms error in determining the positions of the fiducials. FRE is the rms distance between corresponding fiducials after registration and transformation. We have developed a technique for estimating FLE from FRE [43]. The method assumes that the error in determining the positions of the fiducials is an unbiased and uncorrelated random variable, and that FLE is the same in

the two images (i.e., CT and MR). By using this method, we estimated that the FLE for our markers in the images used in this paper is approximately 0.4 mm. We can compare this with three other observations.

- We have previously estimated FLE by means of phantom experiments [44]. For the markers and image protocols used in this study, the experimentally estimated FLE is approximately 0.3–0.4 mm. This FLE is a true measure of accuracy (as opposed to reproducibility) since in these experiments localized image positions were registered to physically known positions.
- We have previously estimated FLE by means of numerical simulations [55]. For the marker shape and size, image voxel dimensions, and image signal-to-noise ratio (SNR) in our study, the predicted FLE is approximately 0.2 mm.
- The FLE of infinitely small markers whose locations within voxels are randomly (uniformly) distributed is

$$\text{FLE} = \sqrt{\frac{\Delta x_v^2 + \Delta y_v^2 + \Delta z_v^2}{12}}$$

which is 1.2 (CT) and 1.3 (MR) mm for the images used in this study.

In summary, the FLE estimated from clinical trial data in this paper is similar to the FLE estimated from phantom experiments. It is slightly higher than the FLE predicted by numerical simulations, probably because of imperfect marker segmentation. It is considerably better than the theoretical FLE of infinitely small markers, demonstrating the advantage of larger markers in producing smaller FLE's [5], [9].

MR images frequently have spatial intensity inhomogeneities due to machine imperfections. Interslice intensity variability is sometimes as high as 10%. Since our technique uses image intensity as a weight when determining the fiducial centroid position, the accuracy of our technique will be affected by intensity distortion. We are currently investigating the use of recently published techniques that correct for MR intensity distortion [11], [56].

Though the algorithm has been written generally so that it will work with arbitrary voxel dimensions, we note that we have tested it only on CT and MR image volumes with slice thickness  $\Delta z_v = 4$  mm. We do not expect that the algorithm will perform well when the largest voxel dimension ( $\Delta z_v$ ) exceeds the shortest marker dimension ( $2r_m$ ). As mentioned above, the parameters  $\alpha$  and  $\beta$  will need to be changed for different voxel dimensions. We look forward to investigating the performance of this algorithm with image volumes that have various voxel dimensions, with different image modalities (e.g., Gradient-Echo MR images), and with different types of markers. For example, the algorithm may be useful for localizing titanium pins that are used to register CT images with physical space in total hip replacement surgery [50], oil pellets that are used to register MR images with neuroelectromagnetic functional images (e.g., equivalent current dipoles and current distributions) [20], or any of the many other external markers that have been used to register 3-D medical images [10], [17]–[19], [30], [33], [47].

Whereas most people use convex markers such as spheres or cylinders, Van den Elsen [52], [54] uses a V-shaped marker. Each leg of the “V” appears as a series of oval marks in the image slices that intersect it. These marks are localized with a semiautomatic algorithm. The fiducial is the vertex of the “V”, calculated as the intersection of two lines fit to the localized marks. An advantage of these markers is that they can be used in image volumes with relatively thick image slices (slice thickness  $> 5$  mm), and with image volumes that have inter-slice gaps. We note that Part One and a 2-D version of Part Two of the algorithm in this paper could be used to fully automate localization of these markers.

The brain can move relative to the skull and thus also to the markers. For example, while the patient is lying in the scanner the brain will settle in the skull. Also, the brain is known to pulsate. Parenchymal excursions in temporal synchrony with systole up to 0.5 mm have been observed [46]. To the extent that the brain moves relative to the skull/markers, the accuracy of the registration of brain tissue will be affected. We note that this is true not only for our marker-based registration method, but for all registration methods based on the skull or something rigidly attached to it, e.g., stereotactic frames. Registration methods based on the skin or something taped or glued to it are even more susceptible to error, since the skin can move relative to the skull/markers as well as the brain.

## VI. CONCLUSION

We have presented a fast, automatic, knowledge-based technique for finding and localizing the centroids of markers externally attached to the head in CT and MR image volumes. The technique is reliable and accurate. We have applied the technique to CT and MR scans from a series of six patients. The image voxel size for each patient is  $0.65 \times 0.65 \times 4.00$  mm for CT and  $1.25 \times 1.25 \times 4.00$  mm for MR. For the CT images the false marker rate was zero. For MR the false marker rate was 1.4% (2 out of 144 markers). The CT-to-MR fiducial registration error averaged 0.4 mm and was better than 0.6 mm for each of the eighteen image pairs.

## ACKNOWLEDGMENT

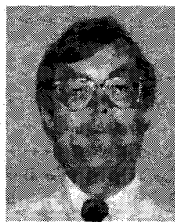
The authors wish to thank J. J. McCrory for contributing to the design and manufacture of the markers, R. R. Price for writing the reverse readout gradient pulse sequences, and S. Gadamsetty for helping collect the patient image data.

## REFERENCES

- [1] L. Adams, W. Krybus, D. Meyer-Ebrecht, R. Rueger, J. M. Gilsbach, R. Moesges, and G. Schloendorff, “Computer-assisted surgery,” *IEEE Comput. Graphics Applicat.*, vol. 10, pp. 43–51, 1990.
- [2] P. E. Anuta, “Spatial registration of multispectral and multitemporal digital imagery using fast fourier transform techniques,” *IEEE Trans. Geosci. Electron.*, vol. GE-8, pp. 353–368, 1970.
- [3] K. S. Arun, T. S. Huang, and S. D. Blostein, “Least-squares fitting of two 3-D point sets,” *IEEE Trans. Pattern Anal. Machine Intell.*, vol. PAMI-9, pp. 698–700, 1987.
- [4] D. I. Barnea and H. F. Silverman, “A class of algorithms for fast image registration,” *IEEE Trans. Comput.*, vol. C-21, pp. 179–186, 1972.

- [5] C. B. Bose and I. Amir, "Design of fiducials for accurate registration using machine vision," *IEEE Trans. Pattern Anal. Mach. Intell.*, vol. 12, pp. 1196–1200, 1990.
- [6] H. Chang, "Geometrical Image Transformation to Compensate for Distortion in Magnetic Resonance Imaging," Ph.D. thesis, Vanderbilt Univ., Nashville, TN, 1990.
- [7] H. Chang and J. M. Fitzpatrick, "A technique for accurate magnetic resonance imaging in the presence of field inhomogeneities," *IEEE Trans. Med. Imag.*, vol. 11, pp. 319–329, 1992.
- [8] Q. Chen, M. Defrise, and F. Deconinck, "Symmetric phase-only matched filtering of Fourier–Mellin transforms for image registration and recognition," *IEEE Trans. Pattern Anal. Machine Intell.*, vol. 16, pp. 1156–1168, 1994.
- [9] G. Chiorboli and G. P. Vecchi, "Comments on 'Design of fiducials for accurate registration using machine vision'," *IEEE Trans. Pattern Anal. Machine Intell.*, vol. 15, pp. 1330–1332, 1993.
- [10] P. Clarysse, D. Gibon, J. Rousseau, S. Blond, C. Vasseur, and X. Marcandise, "A computer-assisted system for 3-D frameless localization in stereotaxic MRI," *IEEE Trans. Med. Imag.*, vol. 10, pp. 523–529, 1991.
- [11] B. Dawant, A. Zijdenbos, and R. Margolin, "Correction of intensity variations in MR images for computer-aided tissue classification," *IEEE Trans. Med. Imag.*, vol. 12, pp. 770–781, 1993.
- [12] E. De Castro and C. Morandi, "Registration of translated and rotated images using finite Fourier transforms," *IEEE Trans. Pattern Anal. Machine Intell.*, vol. PAMI-9, pp. 700–703, 1987.
- [13] L. A. DeSoto, H. S. Choi, D. R. Haynor, Y. Kim, K. J. Burchiel, and T. S. Roberts, "Multiplanar imaging system for stereotaxic neurosurgery," in *Proc. Med. Imag. III: Image Capture and Display*, 1989, vol. 1091, pp. 31–41.
- [14] S. Dong, J. M. Fitzpatrick, and R. J. Maciunas, "Rectification of distortion in MRI for stereotaxic," in *Proc. Fifth Annual IEEE Symp. on Computer based Medical Systems*. Los Alamos, CA: IEEE Computer Society Press, 1992, pp. 181–189.
- [15] V. N. Dvornychenko, "Bounds on (deterministic) correlation functions with application to registration," *IEEE Trans. Pattern Anal. Machine Intell.*, vol. PAMI-5, pp. 206–213, 1983.
- [16] A. C. Evans, S. Marrett, D. L. Collins, and T. M. Peters, "Anatomical-functional correlative analysis of the human brain using three dimensional imaging systems," in *Proc. Med. Imag. III: Image Processing*, 1989, vol. 1092, pp. 264–274.
- [17] A. C. Evans, S. Marrett, J. Torrescorzo, S. Ku, and D. L. Collins, "MRI-PET correlation in three dimensions using a volume-of-interest (VOI) atlas," *J. Cereb. Blood Flow Metab.*, vol. 11, pp. A69–A78, 1991.
- [18] A. C. Evans, T. M. Peters, D. L. Collins, C. J. Henri, S. Marrett, G. B. Pike, and W. Dai, "3-D correlative imaging and segmentation of cerebral anatomy, function and vasculature," *Automed.*, vol. 14, pp. 65–80, 1992.
- [19] E. M. Friets, J. W. Strohbehn, J. F. Hatch, and D. W. Roberts, "A frameless stereotaxic operating microscope for neurosurgery," *IEEE Trans. Biomed. Eng.*, vol. 36, pp. 608–617, 1989.
- [20] M. Fuchs, H.-A. Wischmann, M. Wagner, and J. Krüger, "Coordinate system matching for neuromagnetic and morphological reconstruction overlay," *IEEE Trans. Biomed. Eng.*, vol. 42, pp. 416–420, 1995.
- [21] R. L. Galloway, Jr., C. A. Edwards, II, J. T. Lewis, and R. J. Maciunas, "Image display and surgical visualization in interactive image-guided neurosurgery," *Opt. Eng.*, vol. 32, pp. 1955–1962, 1993.
- [22] R. L. Galloway, Jr., R. J. Maciunas, W. A. Bass, and D. Crouch, "An optical device for interactive, image-guided neurosurgery," in *Proc. Annu. Int. Conf. IEEE Eng. Med. Biol. Soc.*, 1993, vol. 15, pp. 954–955.
- [23] R. L. Galloway, Jr., R. J. Maciunas, and C. A. Edwards, II, "Interactive image-guided neurosurgery," *IEEE Trans. Biomed. Eng.*, vol. 39, pp. 1226–1231, 1992.
- [24] C. A. Glasbey, "An analysis of histogram-based thresholding algorithms," *CVGIP: Graphical Models and Image Processing*, vol. 55, pp. 532–537, 1993.
- [25] A. Goshtasby, "Template matching in rotated images," *IEEE Trans. Pattern Anal. Mach. Intell.*, vol. 7, pp. 338–344, 1985.
- [26] E. M. Haacke, J. Mitchell, and D. Lee, "Improved contrast at 1.5 Tesla using half-Fourier imaging: Application to spin-echo and angiographic imaging," *Magn. Reson. Imag.*, vol. 8, pp. 79–90, 1990.
- [27] D. L. G. Hill, D. J. Hawkes, J. E. Crossman, M. J. Gleeson, T. C. S. Cox, E. E. C. M. L. Bracey, A. J. Strong, and P. Graves, "Registration of MR and CT images for skull base surgery using point-like anatomical features," *Br. J. Radiol.*, vol. 64, pp. 1030–1035, 1991.
- [28] D. Jones, D. A. Christopherson, J. E. Raisis, and J. J. Travaglini, "The use of an external reference system in brain implants," *Endocrine Hypertherm. Oncol.*, vol. 5, pp. 221–226, 1989.
- [29] L. Junck, J. G. Moen, G. D. Hutchins, M. B. Brown, and D. E. Kuhl, "Correlation methods for the centering, rotation, and alignment of functional brain images," *J. Nucl. Med.*, vol. 31, pp. 1220–1226, 1990.
- [30] A. Kato, T. Yoshimine, T. Hayakawa, Y. Tomita, T. Ikeda, M. Mitomo, K. Harada, and H. Mogami, "A frameless, armless navigational system for computer-assisted tomography," *J. Neurosurg.*, vol. 74, pp. 845–849, 1991.
- [31] J. Kittler and J. Illingworth, "On threshold selection using clustering criterion," *IEEE Trans. Syst. Man Cybern.*, vol. SMC-15, pp. 652–655, 1985.
- [32] J. Kittler, J. Illingworth, and J. Föglein, "Threshold selection based on a simple image statistic," *Comput. Vision Graphics Image Processing*, vol. 30, pp. 125–147, 1985.
- [33] Y. Kosugi, E. Watanabe, J. Goto, T. Watanabe, S. Yoshimoto, K. Takakura, and J. Ikebe, "An articulated neurosurgical navigation system using MRI and CT images," *IEEE Trans. Biomed. Eng.*, vol. 35, pp. 147–152, 1988.
- [34] R. J. Maciunas, Ed., *Interactive Image-Guided Neurosurgery*. Park Ridge, IL: Amer. Assoc. of Neurological Surgeons, 1993.
- [35] V. R. Mandava, "Three dimensional multimodal image registration using implanted markers," Ph.D. thesis, Vanderbilt Univ., Nashville, TN, 1991.
- [36] V. R. Mandava, J. M. Fitzpatrick, C. R. Maurer, Jr., R. J. Maciunas, and G. S. Allen, "Registration of multimodal volume head images via attached markers," in *Proc. SPIE, Med. Imag. VI: Image Processing*, 1992, vol. 1652, pp. 271–282.
- [37] P. Margosian, F. Schmitt, and D. Purdy, "Faster MR imaging: Imaging with half the data," *Health Care Instrum.*, vol. 1, pp. 195–197, 1986.
- [38] C. R. Maurer, Jr., G. B. Aboutanos, B. M. Dawant, S. Gadamssetty, R. A. Margolin, R. J. Maciunas, and J. M. Fitzpatrick, "Effect of geometrical distortion correction in MR on image registration accuracy," in *Proc. SPIE, Med. Imag. 1994: Image Processing*, 1994, vol. 2167, pp. 200–213.
- [39] ———, "Effect of geometrical distortion correction in MR on image registration accuracy," to appear in *J. Comput. Assist. Tomogr.*, vol. 20, 1996, in press.
- [40] C. R. Maurer, Jr. and J. M. Fitzpatrick, "A review of medical image registration," in *Interactive Image-Guided Neurosurgery*, R. J. Maciunas, Ed. Park Ridge, IL: Amer. Assoc. of Neurological Surgeons, 1993, pp. 17–44.
- [41] C. R. Maurer, Jr., J. M. Fitzpatrick, R. L. Galloway, Jr., M. Y. Wang, R. J. Maciunas, and G. S. Allen, "The accuracy of image-guided neurosurgery using implantable fiducial markers," in *Computer Assisted Radiology 1995*, H. U. Lemke, K. Inamura, C. C. Jaffe, and M. W. Vannier, Eds. Berlin: Springer-Verlag, 1995, pp. 1197–1202.
- [42] C. R. Maurer, Jr., J. M. Fitzpatrick, M. Y. Wang, and R. J. Maciunas, "Correction of geometrical distortion in MR image registration," in *Proc. Annu. Int. Conf. IEEE Eng. Med. Biol. Soc.*, 1993, vol. 15, pp. 122–123.
- [43] ———, "Estimation of localization accuracy for markers in multimodal volume images," *Proc. Annu. Int. Conf. IEEE Eng. Med. Biol. Soc.*, 1993, vol. 15, pp. 124–125.
- [44] C. R. Maurer, Jr., J. J. McCrory, and J. M. Fitzpatrick, "Estimation of accuracy in localizing externally attached markers in multimodal volume head images," in *Proc. SPIE, Med. Imag. 1993: Image Processing*, 1993, vol. 1898, pp. 43–54.
- [45] N. Otsu, "A threshold selection method from gray-level histogram," *IEEE Trans. Syst. Man Cybern.*, vol. SMC-8, pp. 62–66, 1978.
- [46] B. P. Poncelet, V. J. Wedeen, R. M. Weisskoff, and M. S. Cohen, "Brain parenchyma motion: Measurement with cine echoplanar MR imaging," *Radiol.*, vol. 185, pp. 645–651, 1992.
- [47] D. W. Roberts, J. W. Strohbehn, J. F. Hatch, W. Murray, and H. Kettenberger, "A frameless stereotaxic integration of computerized tomographic imaging and the operating microscope," *J. Neurosurg.*, vol. 65, pp. 545–549, 1986.
- [48] P. K. Sahoo, S. Soltani, A. K. C. Wong, and Y. C. Chen, "A survey of thresholding techniques," *Comput. Vision Graphics Image Processing*, vol. 41, pp. 233–260, 1988.
- [49] T. Takizawa, "A neurosurgical navigation system employing MR images," *Toshiba Med. Rev.*, vol. 34, pp. 10–18, 1990.
- [50] R. H. Taylor, B. D. Mittelstadt, H. A. Paul, W. Hanson, P. Kazanzides, J. F. Zuhars, B. Williamson, B. L. Musits, E. Glassman, and W. L. Bargar, "An image-directed robotic system for precise orthopaedic surgery," *IEEE Trans. Robot. Automat.*, vol. 10, pp. 261–275, 1994.
- [51] Q. Tian and M. N. Huhns, "Algorithms for subpixel registration," *Comput. Vision Graphics Image Processing*, vol. 35, pp. 220–233, 1986.
- [52] P. A. Van den Elsen, "Multimodality Matching of Brain Images," Ph.D. thesis, Utrecht Univ., Utrecht, Netherlands, 1993.

- [53] P. A. Van den Elsen, E.-J. D. Pol, and M. A. Viergever, "Medical image matching: A review with classification," *IEEE Eng. Med. Biol. Mag.*, vol. 12, pp. 26-39, 1993.
- [54] P. A. Van den Elsen, M. A. Viergever, A. C. Van Huffelen, W. Van der Meij, and G. H. Wieneke, "Accurate matching of electromagnetic dipole data with CT and MR images," *Brain Topogr.*, vol. 3, pp. 425-432, 1991.
- [55] M. Y. Wang, J. M. Fitzpatrick, and C. R. Maurer, Jr., "Design of fiducials for accurate registration of CT and MR volume images," in *Proc. SPIE, Med. Imag. 1995: Image Processing*, 1995 vol. 2434, pp. 96-108.
- [56] W. M. Wells, III, W. E. L. Grimson, R. Kikinis, and F. A. Jolesz, "Statistical intensity correction and segmentation of MRI data," in *Proc. SPIE, Visualization Biomed. Comput.*, 1994, vol. 2359, pp. 13-24.



**J. Michael Fitzpatrick (M'94)** was born in Topeka, KS, in 1945 and received the B.S. degree in physics from the University of North Carolina, Chapel Hill, NC, in 1967, the Ph.D. degree in physics from the Florida State University, Tallahassee, FL, in 1972, and the M.S. degree in computer science at the University of North Carolina, Chapel Hill, NC, in 1982.

He has been an Associate Professor in the Departments of Computer Science, Neurosurgery, and Radiology at Vanderbilt University, Nashville, TN, since 1982 where he heads a research group in medical imaging and image registration. His current research interests include image-guided neurosurgical navigation, inter-modality image registration, and magnetic resonance image rectification.



**Matthew Y. Wang (S'93)** received the B.S. degree in electrical engineering from Electronic Science and Technology University of China, Xi'an, in 1988, and the M.S. degree in electrical engineering from Zhejiang University, Hangzhou, China, in 1990. He is pursuing the Ph.D. degree in computer science at Vanderbilt University, Nashville, TN.

His past research work focused on local area networks, neural networks, real-time image processing, parallel processing, and knowledge-based image understanding systems. His current interests

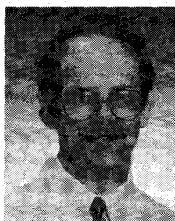
include medical image acquisition, localization, and registration, and the use of registered images in stereotactic neurosurgery and stereotactic radiosurgery.



**Calvin R. Maurer, Jr. (S'93)** received the B.S.E. degree in chemical engineering from Princeton University, Princeton, NJ, in 1980, and the M.S. degree in biomedical engineering from Vanderbilt University, Nashville, TN, in 1993. He is working on the Ph.D. degree in biomedical engineering at Vanderbilt.

His past work focused on the use of mathematical models to study cardiac mechanics and pulmonary microvascular transport phenomena. His current research interests include medical image registration

and interactive image-guided neurosurgery.



**Robert J. Maciunas** received the B.A. degree in chemistry, and the B.A. degree in biology at Northwestern University, Evanston, IL. He attended the University of Illinois at Chicago Medical School and completed a surgical internship, neurosurgical residency, and fellowships in cerebrovascular neurosurgery and stereotactic neurosurgery at the Mayo Clinic, Rochester, MN.

He is Associate Professor of Neurological Surgery at Vanderbilt University, Nashville, TN. He is Chief of the Neurosurgery Service at the Nashville Veteran's Administration Hospital, Director of the Computerized Photon Knife Program, and Director of the Brain Tumor Center at Vanderbilt. He is author of more than 60 scientific articles and editor of the book *Interactive Image-Guided Neurosurgery* (Park Ridge, IL: Amer. Assoc. Neurological Surgeons, 1993). His current research interests include computer assisted navigation systems for surgery, neurosurgical applications of the medical free electron laser, and regionally determined variations in the cell biology of growth factors in glial tumors.